

# A CNN-based Spatial Feature Fusion Algorithm for Hyperspectral Imagery Classification

Alan J.X. Guo, Fei Zhu \*

June 14, 2022

## Abstract

The shortage of training samples remains one of the main obstacles in applying the artificial neural networks (ANN) to the hyperspectral images classification. To fuse the spatial and spectral information, pixel patches are often utilized to train a model, which may further aggregate this problem. In the existing works, an ANN model supervised by center-loss (ANNC) was introduced. Training merely with spectral information, the ANNC yields discriminative spectral features suitable for the subsequent classification tasks. In this paper, a CNN-based spatial feature fusion (CSFF) algorithm is proposed, which allows a smart fusion of the spatial information to the spectral features extracted by ANNC. As a critical part of CSFF, a CNN-based discriminant model is introduced to estimate whether two paring pixels belong to the same class. At the testing stage, by applying the discriminant model to the pixel-pairs generated by the test pixel and its neighbors, the local structure is estimated and represented as a customized convolutional kernel. The spectral-spatial feature is obtained by a convolutional operation between the estimated kernel and the corresponding spectral features within a neighborhood. At last, the label of the test pixel is predicted by classifying the resulting spectral-spatial feature. Without increasing the number of training samples or involving pixel patches at the training stage, the CSFF framework achieves the state-of-the-art by declining 20% – 50% classification failures in experiments on three well-known hyperspectral images.

## 1 Introduction

A hyperspectral image is a collection of spectral pixels. Each of them records a continuous reflection spectrum over a same land-cover, with hundreds of channels across a certain wavelength range. The classification of these spectral pixels is a natural and essential task in hyperspectral images analysis [1].

To address the classification task, an amount of spectrum-based works are proposed. Among, linear algorithms in dimension reduction and feature classification are the most investigated, for example, the principal component analysis (PCA) [2], the independent component analysis (ICA) [3] and the linear discriminant analysis (LDA) [4]. Nonlinear methods are also introduced to achieve better representations of the spectra, including but not limited to the support vector machine (SVM) [5], the manifold learning [6] and the kernel-based algorithms [7, 8], to name a few.

With the increasing imaging qualities of both spectral and spatial resolutions [9], the spectral-spatial algorithms for accurate classification have gained much attention [10–15]. Specifically, a multi-scale adaptive sparse representation (MASR) method is proposed in [16], where the spatial information at different scales is exploited simultaneously. In MASR, each neighboring pixel is represented via an adaptive sparse combination of training samples, and the label of the centering test pixel is determined by the recovered sparse coefficients. It is noteworthy that although MASR utilizes the spatial information at the testing stage, only spectral samples are engaged at the training stage. This strategy helps to alleviate the shortage of training data to some degree.

Since the artificial neural networks (ANN) and the convolutional neural networks (CNN) were proposed, these models have been successfully applied in many fields related to machine learning and signal processing [17–20]. Recently, the ANN and CNN models have been introduced to hyperspectral images classification and achieved improvements over the traditional methods in terms of classification accuracy. Earlier works include the stacked

---

\* Alan J.X. Guo and Fei Zhu are with the Center for Applied Mathematics, Tianjin University, China. (jiaxiang.guo;fei.zhu@tju.edu.cn)

autoencoder (SAE) [21, 22], the deep belief network (DBN) [23] and *etc..* More recently, many of the researchers focus on the varieties of CNN-based models. Trials have been made with impressive advances, as studied in [24–32].

Training with pixel patches is a natural idea to take advantage of both spectral and spatial information, and is adopted by most of the aforementioned ANN or CNN based studies [24–32]. However, it should be noticed that this strategy may further aggravate the shortage of training data. Different from the numerous accessible RGB images, the labeled samples are limited in hyperspectral imagery, which are usually insufficient for network training [25]. Compared with the spectrum-based models, the pixel-patch-based ones aggregate this contradiction from two aspects,

- using pixel patches often complicates the model by introducing additional undetermined parameters, thus requiring more training data;
- a hyperspectral image usually contains fewer mutually non-overlapped patches with specified size than pixel-wise samples.

Several attempts have been made to overcome the shortage of training data, such as the virtual sample strategy [25], the pre-training and fine-tuning techniques [30, 31].

Moreover, to circumvent the obstacle raised by training with pixel patches, frameworks are built by concatenating a spectrum-based model and a post spatial information integration scheme. Following this idea, the pixel-pair feature algorithm (PPF) [33] and the ANNC with adaptive spatial-spectral center classifier (ANNC-ASSCC) [32] have been proposed in the literature. Together with the aforementioned MASR algorithm, the three methods are chosen to be compared with the proposed CSFF algorithm in the experiments, as to be reported in Section 3.

The PPF framework presented a pixel-pair-based classification model using CNN. Let  $x_1$  and  $x_2$  be two pixels with label  $\ell(x_1)$  and  $\ell(x_2)$ , respectively. The pixel-pair for training is generated as  $(x_1, x_2)$ , with the label determined by

$$\ell((x_1, x_2)) = \begin{cases} \ell(x_1) & \text{if } \ell(x_1) = \ell(x_2), \\ 0 & \text{otherwise.} \end{cases}$$

It is observed that the number of pixel-pairs computes  $C_N^2$ , where  $N$  is the size of the training set. This enlarged size of the training set enables the training of a deep CNN model. The model classifies the pixel-pairs into  $K + 1$  classes with labels 0 and  $1, 2, \dots, K$ , where  $K$  is the number of pixel classes. At the testing stage, pixel-pairs are firstly generated by the test pixel and its neighbors, and then classified into  $K + 1$  classes by the learned CNN model. The final label of a test pixel is determined by a voting strategy among the non-zero classification results.

In [32], an ANN-based feature extraction and classification framework is proposed. The so-called ANNC-ASSCC algorithm consists of two successive steps:

- spectral feature extraction with ANN;
- adaptive spatial information fusion and classification.

In the first step, a simple but efficient ANN structure is designed to extract spectral features. As illustrated in Fig. 1, the network contains 4 fully connected layers, and a joint supervision of softmax loss and center loss is applied for classification task. During the training stage, the  $k$  class centers, *i.e.*  $c_1, c_2, \dots, c_k$ , are updated by averaging the 3rd layer's outputs within respective classes. For a training pixel, the introduced center loss encourages the output of 3rd layer to gather around its corresponding class center in Euclidean space. At the testing stage, the first 3 layers of the learned network are utilized and the outputs of the 3rd layer are regarded as the extracted spectral features. In the second step, the spatial information is merged by averaging the extracted spectral features within neighboring regions of different sizes. After the resulting features are classified, a voting strategy is applied to generate the final prediction.

In this paper, we choose the ANNC in [32] as the spectral feature extraction model, and design a CNN-based Spacial Feature Fusion (CSFF) algorithm to posteriorly integrate the spatial information. The main characters of the proposed classification framework are listed as below.

1. Rather than implicit spatial information utilized in [32], explicit spatial structures are produced by our novel CNN-based model. Therefore, the CSFF works more reasonably than the averaging fusion strategy in the previous work [32].

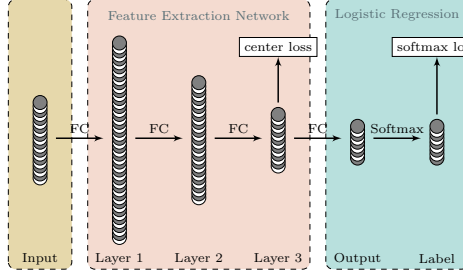


Figure 1: Structure of the spectral feature extracting network. [32]

2. The CSFF algorithm shares the same training data with the spectral feature extraction model, which is chosen as ANNC in this paper. Without increasing the size of the training set, this settlement keeps the whole framework working on a small amount of training data.
3. To enhance the representative ability of the framework, the spatial structure extraction algorithm in CSFF is designed to have a totally different network structure from ANNC, such that the two models are distinguished at feature expression and abstraction levels. To be precise, the ANNC expresses shallow features of spectra, while the spatial structure extraction algorithm produces more abstract features with a deeper and more complex model structure. This helps to alleviate the correlation between these two models, thus increasing the performance of the whole framework.

Benefiting the above characters, without requiring more training data, the proposed CSFF algorithm allows to achieve the state-of-the-art by declining 20% – 50% classification failures in experiments.

The reminder of this paper is organized as follows. The whole framework outline and the CSFF algorithm are discussed in Section 2. Section 3 reports the experimental results and analysis. In Section 4, some concluding remarks are presented.

## 2 Framework outline and the CNN-based spatial feature fusion algorithm

In this section, we present an end-to-end spectral-spatial feature extraction and classification framework. The whole structure is firstly outlined, with detailed explanations on each of the three components. As a key ingredient of the whole framework, the CSFF algorithm is introduced with emphasis placed on the newly proposed CNN-based discriminant model, which outputs the predicted probability of two pixels belonging to the same class.

### 2.1 Framework outline

As discussed previously, training with pixel patches may further aggregate the lack of labeled samples. Based on this concern, the training stage of the proposed framework is performed merely using the spectral data, while the spatial information is involved posteriorly at the testing stage. The proposed framework is designed to consist of three parts, namely

- spectral feature extraction;
- spatial structure extraction and fusion of spectral feature and spatial structure;
- classification of the spectral-spatial feature.

The flowchart of the whole framework is given in Fig. 2.

In the first part, we extract the spectral features of the whole hyperspectral image by directly applying the ANNC model proposed in [32]. This spectrum-based model is supervised with a joint loss of center loss and softmax loss, producing discriminative spectral features with inner-class compactness and inter-class variations. Taking advantage of this, the spectral features obtained by the learned ANNC model is suitable for the successive

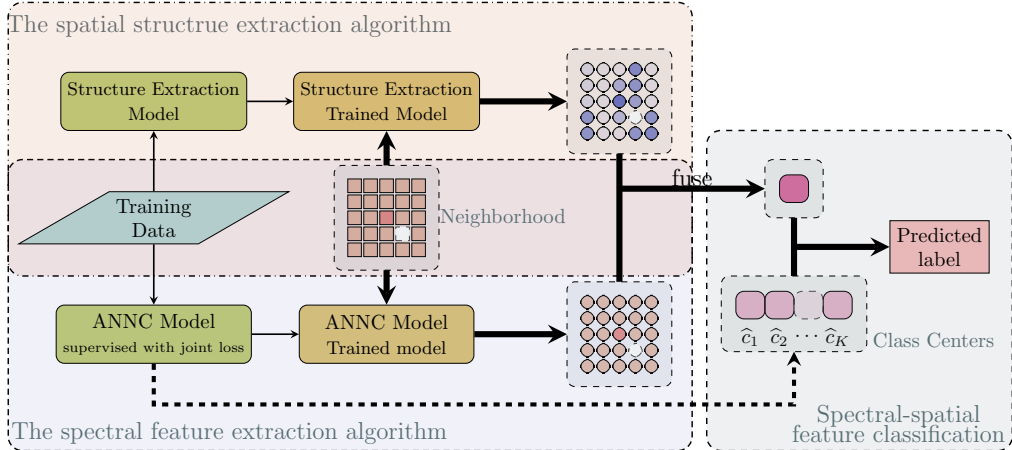


Figure 2: Flowchart of the proposed framework. The three components are represented by three dashed rectangles. The training and testing stages are distinguished by thin and thick solid arrows, respectively. The dashed arrows represent the estimation of class centers of features. The intersection of neighborhood and training samples are represented by the white pixel, and are excluded at the testing stage.

spatial information fusion step. In the following, we use the notations  $x$  and  $f_{\text{ANNC}}(x)$  to denote a given pixel and its corresponding spectral feature extracted by the ANNC model, respectively.

In the second part, the spatial structure extraction algorithm is designed to explore the local structure for a given pixel within some pre-defined neighborhood. More precisely, the local structure is characterized by a customized ‘‘convolutional kernel’’. The fusion of the spectral-spatial information is realized by a ‘‘convolutional’’ operation between the kernel and the extracted spectral features within the neighborhood. Let  $N(x)$  be a neighborhood centering at pixel  $x$  and  $W(N(x))$  be the customized ‘‘convolution kernel’’. Use the notation  $f_{\text{ANNC}}(N(x))$  to represent the data cube formed by the extracted spectral features within the neighborhood  $N(x)$ , where the  $i, j$ -th entry is defined by

$$f_{\text{ANNC}}(N(x))_{i,j} = f_{\text{ANNC}}(N(x)_{i,j}).$$

Using  $f_{N(x)}(x)$  to denote the spectral-spatial feature of  $x$  within the neighborhood  $N(x)$ , it is defined by

$$f_{N(x)}(x) = W(N(x)) \otimes f_{\text{ANNC}}(N(x)), \quad (1)$$

where  $\otimes$  indicates the convolutional operation. A more clear interpretation of this model will be given in Section 2.2.

The last part of the framework aims to classify the resulting spectral-spatial feature  $f_{N(x)}(x)$ . In [32], a center classifier is introduced, which assigns the label to each sample according to its nearest class center. Let  $\hat{c}_1, \hat{c}_2, \dots, \hat{c}_k$  be the class centers estimated from the extracted spectral features of the training set. The label of the spectral-spatial feature  $f_{N(x)}(x)$  is predicted by

$$\ell(f_{N(x)}(x)) = \arg \min_i \{ \|f_{N(x)}(x) - \hat{c}_i\|_2\}. \quad (2)$$

Experiments in Section 3.2 show that the spectral-spatial features are not sensitive to the applied classifiers, that similar classification accuracies are obtained by using the center classifier, the support vector machine (SVM) algorithm, and the  $k$ -nearest neighbors ( $k$ NN) algorithm. However, the center classifier is still the simple and straightforward one, and is engaged as the default classifier in the proposed framework.

## 2.2 Spatial structure extraction algorithm

The most crucial aspect of CSFF is the spatial structure extraction algorithm. This algorithm relies on a CNN-based discriminant network, which is designed to predict the probability that an input pair of pixels have the same label. By applying this model to the pixel-pairs generated by the test pixel and its neighbors, the corresponding local spatial structure can be extracted and represented as a matrix that maps the neighborhood. The procedure

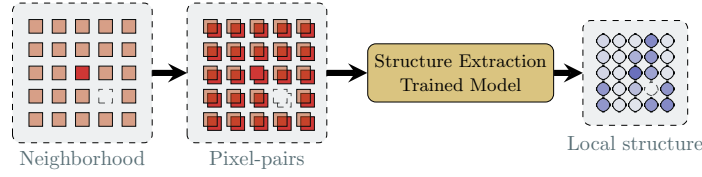


Figure 3: Flowchart of the spatial structure extraction algorithm. Pixel pairs are firstly generated by the center pixel and its neighbors and then fed into the model. For each pixel-pair, the model predicts the probability that the two elements share the same class label. The spatial structure is extracted as the output of this discriminant model.

is illustrated in Fig. 3. To be more precise, use  $D((x, x'))$  to denote the predicted probability that the entries of pixel-pair  $(x, x')$  have the same class label. Let  $\{x\} \times N(x) = \{(x, x') | \forall x' \in N(x)\}$  be a set of pixel-pairs generated by the centering pixel  $x$  and its neighbors within  $N(x)$ , we use  $D(\{x\} \times N(x))$  to denote the corresponding spatial matrix, whose  $i, j$ -th entry is defined by

$$D(\{x\} \times N(x))_{i,j} = D((x, N(x)_{i,j})).$$

By applying an element-wise threshold function  $f_t$ , the real-valued  $D(\{x\} \times N(x))$  is calibrated to a binary matrix

$$D_t(\{x\} \times N(x)) = f_t(D(\{x\} \times N(x))),$$

where  $t$  is the pre-determined threshold value. The convolutional kernel  $W(N(x))$  in (1) is calculated by normalizing  $D_t(\{x\} \times N(x))$  such that all the elements add up to a unit.

To enhance the hierarchical representative capability of the whole framework, the aforementioned discriminant model is designed to extract the deep features, while the spectral feature extraction model (the ANNC) focuses on exploring the shallow features with a simple network structure. From this point of view, distinguished architecture and structure are considered to make the proposed discriminant model different from ANNC, namely

1. While the ANNC uses a structure of fully connected layers, the CNN architecture will be employed in the discriminant model. A CNN-based model is not only built differently from ANNC model, but is also expected to be more powerful in expressing hierarchical features.
2. While the ANNC uses a shallow structure of 3 layers, a deep model with more layers will be engaged in the discriminant model. In most cases, deep networks enable the extraction of more abstract features than the respectively shallow ones.

It is noteworthy that training a complex discriminant model with a limited number of labeled pixels is possible. To address the task of distinguishing whether two spectra belong to the same class, the discriminant model is designed to be fed with pixel-pairs at both training and testing stage. Without considering the geometric information, the pixel-pairs for training are generated by the pixels chosen from training data. According to this settlement, the training set can be enlarged to roughly have a squared quantity of training samples. In practice, the enlarged training set is sufficient for training our discriminant model.

Based on above discussions, we choose to modify the pixel-pair features (PPF) model proposed in [33] and use the resulting network as the discriminant model in our spatial structure extraction algorithm. The PPF is a CNN-based framework proposed for multi-classification task. The authors designed this model for classifying pixel-pairs into  $K + 1$  classes, which are

- class  $i$ , if two pairing pixels are from the same class  $i$ , for  $1 \leq i \leq K$ ;
- class 0, otherwise.

The pixel-pair strategy is applied for alleviating the shortage of training data.

Fortunately, the PPF model is not only CNN-based, but also has a relatively deep structure of 9 convolutional or fully connected layers and 3 pooling layers. This meets the directions discussed above for structure design of our

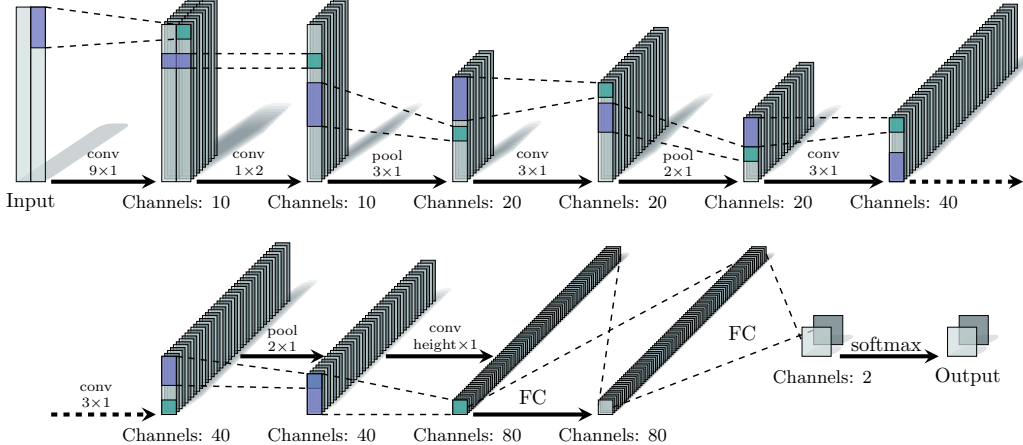


Figure 4: Structure of the discriminant model. The sizes of convolution kernels are marked under the layer type conv, while the cardinalities of channels are presented under the graphical data blobs. In fact, each channel of a preceding data blobs is connected to all the channels of latter data blobs in the convolutional layers, but only one connection is drawn for simplicity.

discriminant model. Moreover, the binary classification task is relatively easier than the original multi-classification task and should be expressed well by a similar model with PPF. By modifying the first data layer and the last two fully connected layers, the structure is able to address different datasets and is suitable for the binary classification task. The modified structure of PPF model is applied as our discriminant model, which is a part of the spatial feature extraction algorithm.

The structure details of the discriminant model are illustrated in Fig. 4. Considering the slim shape of the input data, namely  $(2, L)$ , with  $L$  being the number of spectral channels, the convolution kernels and the pooling area are chosen as narrow rectangular ones instead of the traditional square ones. All the strides of the convolutional layers are set to be 1 and the pooling layers are defined to use the max-pooling function. In order to introduce nonlinearity to the CNN-based model, the commonly-used rectified linear unit (ReLU) function, defined by  $\phi(x) = \max\{0, x\}$ , is applied after every convolutional and fully connected layer.

### 3 Experimental settings and result analysis

In this section, the performance of the proposed CSFF algorithm is validated by comparing it with the aforementioned state-of-the-art methods, on classifying three well-known hyperspectral images. The datasets are firstly introduced, followed by a description on experimental settings. An analysis of the classification results is also reported.

#### 3.1 Descriptions of the datasets

Experiments are performed on three real hyperspectral images, namely the Pavia University scene, the Salinas scene, and the Pavia Centre scene\*.

The first data is the Pavia University scene, acquired by the Reflective Optics System Imaging Spectrometer (ROSIS) sensor. After removing the noisy bands and a blank strip, a sub-image of  $610 \times 340$  pixels with 103 spectral bands are retained for analysis. The image is characterized by a spatial resolution of about 1.3 meters. As summarized in TABLE 1, this area is known to be mainly composed by  $K = 9$  classes of materials, denoted by labels from 1 to 9. The background pixels are represented by label 0, and will not be taken into account for classification. Fig. 5 presents the false color composite and groundtruth map.

The second one is the Salinas scene collected by the Airborne Visible Infrared Imaging Spectrometer (AVIRIS). This dataset contains  $512 \times 217$  pixels, and is characterized by a resolution of 3.7 meters. After removing the

\*The datasets are available online: [http://www.ehu.eus/ccwintco/index.php?title=Hyperspectral\\_Remote\\_Sensing\\_Scenes](http://www.ehu.eus/ccwintco/index.php?title=Hyperspectral_Remote_Sensing_Scenes)

Table 1: Reference classes and sizes of training and testing sets of Pavia University image

No.	Class	Cardinality	Train	Test
1	Asphalt	6631	200	6431
2	Meadows	18649	200	18449
3	Gravel	2099	200	1899
4	Trees	3064	200	2864
5	Painted metal sheets	1345	200	1145
6	Bare Soil	5029	200	4829
7	Bitumen	1330	200	1130
8	Self-Blocking Bricks	3682	200	3482
9	Shadows	947	200	747
Total		42776	1800	40976

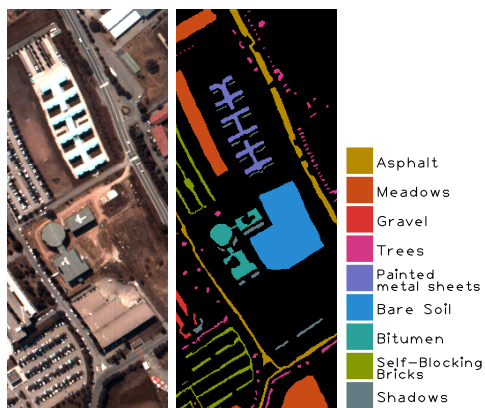


Figure 5: The false color composite (band 10, 20, 40) and groundtruth representation of Pavia University

Table 2: Reference classes and sizes of training and testing sets of Salinas image

No.	Class	Cardinality	Train	Test
1	Brocoli green weeds 1	2009	200	1809
2	Brocoli green weeds 2	3726	200	3526
3	Fallow	1976	200	1776
4	Fallow rough plow	1394	200	1194
5	Fallow smooth	2678	200	2478
6	Stubble	3959	200	3759
7	Celery	3579	200	3379
8	Grapes untrained	11271	200	11071
9	Soil vinyard develop	6203	200	6003
10	Corn senesced green weeds	3278	200	3078
11	Lettuce romaine 4wk	1068	200	868
12	Lettuce romaine 5wk	1927	200	1727
13	Lettuce romaine 6wk	916	200	716
14	Lettuce romaine 7wk	1070	200	870
15	Vinyard untrained	7268	200	7068
16	Vinyard vertical trellis	1807	200	1607
Total		54129	3200	50929

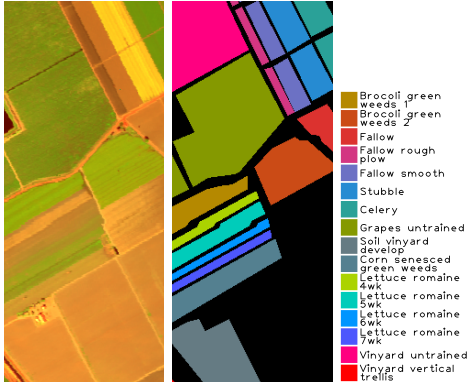


Figure 6: The false color composite (band 180, 100, 10) and groundtruth representation of Salinas

water absorption bands, the remaining 204 (out of 224) bands are utilized. According to the available groundtruth information in TABLE 2, there are  $K = 16$  composition categories of interest, with the background pixels represented by label 0. False color composite and groundtruth map of the Salinas scene are shown in Fig. 6.

The last image is the Pavia Centre scene, which is also returned by the ROSIS sensor over Pavia, northern Italy. A sub-image of  $1096 \times 715$  pixels with 102 relative clean bands is taken into account, where the geometric resolution is 1.3 meters. Ignoring the background pixels, the groundtruth labels fall into  $K = 9$  reference classes, as given in TABLE 3. The false color composite and the groundtruth map of Pavia Center are shown in Fig. 7.

### 3.2 Experimental settings

#### 3.2.1 Training and testing sets

Before further processing, each dataset is firstly normalized to have zero mean and unit variance. To form the training set, 200 pixels are randomly chosen from each class. The two neuron networks, *i.e.*, the ANNC model and discriminant model, are trained by employing the same training set. In TABLES 1–3, the sizes of training and testing sets for datasets Pavia University scene, Salinas scene, and Pavia Centre scene are reported.

To train the ANNC model, the original training set is enlarged by virtual samples [25, 32], until the size of each class reaches 80000. Using  $x_1, x_2$  to denote two training pixels chosen from class  $\ell$ , a virtual sample  $\tilde{x}$  with the

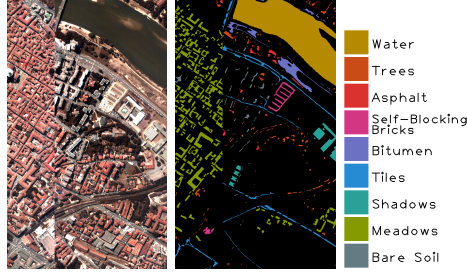


Figure 7: The false color composite (band 10, 20, 40) and groundtruth map of Pavia Centre

same label is generated by  $\tilde{x} = qx_1 + (1 - q)x_2$ , where  $q$  is a random number chosen from the uniform distribution on  $[-1, 2]$ . Note that, compared to the real samples, the variance of virtual ones may be reduced, hence the range of  $q$  is empirically set to be  $[-1, 2]$  instead of  $[0, 1]$ . The testing set consists of all the unused pixels, that are fed into the learned ANNC model directly at the testing stage.

To train the discriminant model in spatial feature extraction algorithm, the pixel-pairs are firstly generated. Let  $Tr_i$  be the set of training pixels with label  $i$ , for  $i = 1, 2, \dots, K$ . The positive training set is expressed by

$$\begin{aligned} Tr_+ &= \bigcup_i Tr_i \times Tr_i \\ &= \bigcup_i \{(x_1, x_2) \mid \forall x_1, x_2 \in Tr_i\}. \end{aligned}$$

The negative training set is generated by taking the Cartesian product between any two different classes of training pixels, namely

$$\begin{aligned} Tr_- &= \bigcup_{i \neq j} Tr_i \times Tr_j \\ &= \bigcup_{i \neq j} \{(x_1, x_2) \mid \forall x_1 \in Tr_i, x_2 \in Tr_j\}. \end{aligned}$$

Considering that the size of negative training set  $Tr_-$  is overwhelmingly greater than that of the positive set  $Tr_+$ , only half of the negative pixel-pairs are randomly chosen for training. At the testing stage, a doubled neighborhood radius will quadruple the computational cost. As aforementioned, the sizes of the Pavia University scene and the Pavia Centre scene are greater than that of the Salinas scene. With limited computing power, the size of neighborhoods are empirically chosen to be  $19 \times 19$  on both the Pavia University scene and the Pavia Centre scene, while the smaller dataset Salinas scene, is tested with a neighborhood size  $39 \times 39$ . It is noteworthy that, the training pixels are excluded from either the testing samples or their neighbors.

Table 3: Reference classes and sizes of training and testing sets of Pavia Centre image

No.	Class	Cardinality	Train	Test
1	Water	65971	200	65771
2	Trees	7598	200	7398
3	Asphalt	3090	200	2890
4	Self-Blocking Bricks	2685	200	2485
5	Bitumen	6584	200	6384
6	Tiles	9248	200	9048
7	Shadows	7287	200	7087
8	Meadows	42826	200	42626
9	Bare Soil	2863	200	2663
Total		148152	1800	146352

### 3.2.2 Network Configurations

As studied in [32], the ANNC network is trained with a joint loss of softmax loss and center loss, where the weight of center loss is set to be  $\lambda = 0.01$ . A stochastic gradient descent (SGD) is applied with learning rate initialized as 0.01 and decays by multiplying 0.3162 every 20000 steps. The size of the mini-batch is set to be 512. This model is implemented on the open source deep learning framework Caffe [34].

In the spatial structure extraction algorithm, a cross entropy loss is introduced after the softmax layer for training the discriminant model. The SGD algorithm is used for optimizing the model, with the mini-batch size set to be 512. Learning rate is initialized with 0.01 and decays every 50 epochs by multiplying 0.1. The training algorithm stops after the learning rate has decayed 3 times. For the sake of using rectangular convolutional kernels, this model is implemented on the compatible machine learning framework Tensorflow [35], following the codes of [33].

### 3.2.3 Configuration of spatial feature extraction algorithm and classifiers

As aforementioned in Section 2.2, a threshold value  $t$  is introduced for tuning the probabilities in  $D(\{x\} \times N(x))$  to predictions in  $D_t(\{x\} \times N(x))$ . It is noteworthy that, although half of the generated negative pixel-pairs are discarded from training data, the weight of negative samples is still times of the positive ones. As a result, the trained discriminant model tends to give negative predictions. To include more information into account, a low threshold value  $t = 0.01$  is chosen in this framework.

To evaluate the performance of the spectral-spatial features  $f_{N(x)}(x)$ , a comparative study is performed by classifying them using three classifiers, namely the center classifier mentioned in (2), the  $k$ NN algorithm [36], and the SVM algorithm [37]. Without involving extra training data, these three classifiers are trained based on the same training pixels as used in training ANNC model and the discriminant model. To be more precise, by applying a transfer learning strategy [38], the classifiers are trained with spectral features (with their respective labels) extracted by the learned ANNC model from the training pixels<sup>†</sup>. In practice, the class centers in center classifier are estimated by averaging the spectral features of training pixels within each class. Concerning  $k$ NN, it assigns a test spectral-spatial feature to the class most common among its  $k$  nearest training spectral features, where two cases with  $k = 5$  and  $k = 10$  are considered in the experiments. Similar to the  $k$ NN algorithm, the SVM algorithm is also trained by the spectral features with their respective labels. The rbf kernel is applied and the multi-class classification is handled according to a one-vs-one scheme. The Python package SciPy is applied directly for  $k$ NN and SVM algorithms, with the parameters, that are not given explicitly here, set to be the default values<sup>‡</sup>.

## 3.3 Results analysis

We evaluate the classification performance of the proposed framework on the aforementioned datasets. In this framework, the models are trained merely based on spectral pixels without using spatial information, as the latter is likely to coincide with the testing set. From this aspect, three state-of-the-art classification methods are considered, which are the traditional method MASR [16], the CNN-based PPF [33], and the ANN-based ANNC-ASSCC [32]. For fair comparison, all the comparative methods are trained with the training sets of same size, namely 200 random pixels for each class.

Three commonly-used metrics are adopted to evaluate the classification performance globally, which are the overall accuracy (OA), the average accuracy (AA), and the Kappa coefficient ( $\kappa$ ). Briefly, OA represents the overall percentage of testing samples that are correctly classified, while AA calculates the average value of the accuracies of each class on testing samples. The  $\kappa$  coefficient measures the agreement between the predicted labels and groundtruth labels.

As illustrated in TABLES 4–6, competitive classification results are obtained by the proposed CSFF method on all the three datasets. On the Pavia University scene, the CSFF provides the best classification accuracy in terms of OA, AA, and  $\kappa$ , which signifies a 20% – 30% drop in prediction failures over the second best ANNC-ASSCC. Similar improvements are also observed on the Salinas scene, where the CSFF yields over 1.5% increase in OA when compared to the ANNC-ASSCC, the value corresponding to around 50% fewer prediction failures.

<sup>†</sup>Here, the spectral-spatial features of the training pixels are not used for training the classifiers, for the sake that no additional information from the pixels other than the training ones should be used before the testing stage. For a given training pixel  $x$ , its neighborhood  $N(x)$  used for spectral-spatial feature generation may contain the pixels from the testing set. Hence, the resulting spectral-spatial feature  $f_{N(x)}(x)$  may contain the information from the testing set, and is not proper for training the classifiers.

<sup>‡</sup>Software available at <https://www.scipy.org/>.

Table 4: Classification accuracies (averaged over 5 runs) of MASR, PPF, ANNC-ASSCC and CSFF on Pavia University scene

	MASR	PPF	ANNC-ASSCC	CSFF
Asphalt	89.97	97.25	98.69	98.46
Meadows	98.78	95.24	99.97	99.79
Gravel	99.78	94.17	93.85	96.03
Trees	97.47	97.20	96.68	98.00
Painted metal sheets	100.00	100.00	100.00	99.96
Bare Soil	99.87	99.37	100.00	100.00
Bitumen	100.00	96.16	96.88	98.91
Self-Blocking Bricks	98.76	93.83	93.11	95.21
Shadows	92.17	99.46	97.62	100.00
OA(%)	97.42	96.25	98.55	98.90
AA(%)	97.42	96.97	97.42	98.49
$\kappa$	0.9654	0.9499	0.9805	0.9852

Specifically, noteworthy improvements are achieved over the methods PPF and ANNC-ASSCC on addressing two difficult classification tasks, *i.e.*, the Grapes untrained and the Vinyard untrained. It is noteworthy that although the MASR obtains the best classification results, one possible reason is that the algorithm does not exclude the training pixels when utilizing the spatial information, as explained in [32]. To this end, a modified version of MASR, termed MASR-t is applied on the Salinas scene for fairness, as given in TABLE 5. Concerning the Pavia Centre scene, the CSFF still leads to slight improvements on all the metrics, considering the high classification accuracies achieved by the comparing counterparts.

The proposed CSFF generates explicit spectral-spatial features that can be classified using different classification algorithms. To examine the effectiveness of the features obtained by the CSFF under various classifiers, experiments are performed by using the default center classifier,  $k$ NN, and SVM, on all the datasets. The results are given in TABLES 7–9. We observe that on all the images, the three classifiers yield stable and similar classification accuracies in terms of all the quantitative metrics. It demonstrates that the spectral-spatial features generated by the proposed framework are effective and robust against different classifiers.

## 4 Conclusion

In this paper, we investigated a novel ANN and CNN based classification framework that properly integrates the spatial information to the spectral-based features, and generates spectral-spatial features appropriate for various classifiers. Based on a limited number of labeled pixels and without using any local information, both a spectral feature extraction model and a discriminant model were trained. Using the learned discriminant model, the local structure was extracted and represented as a customized convolutional kernel. The spectral-spatial feature was obtained by a convolutional operation between the kernel and the corresponding spectral features within a neighborhood. Experiments on three real hyperspectral images validated the performance of the proposed method in terms of classification accuracy, when compared to the state-of-the-art algorithms. We also studied the characteristics of the learning features, which showed robustness and stabilities against various classifiers. Future works will focus on extending the proposed framework to multiple-model fusion.

## References

- [1] D. Lu and Q. Weng, “A survey of image classification methods and techniques for improving classification performance,” *International Journal of Remote Sensing*, vol. 28, no. 5, pp. 823–870, 2007.
- [2] G. Licciardi, P. R. Marpu, J. Chanussot, and J. A. Benediktsson, “Linear versus nonlinear PCA for the classification of hyperspectral data based on the extended morphological profiles,” *IEEE Geoscience and Remote Sensing Letters*, vol. 9, no. 3, pp. 447–451, May 2012.

Table 5: Classification accuracies (averaged over 5 runs) of MASR, PPF, ANNC-ASSCC and CSFF on Salinas

	MASR	MASR-t	PPF	ANNC-ASSCC	CSFF
Brocoli_green_weeds_1	100.00	100.00	100.00	100.00	99.97
Brocoli_green_weeds_2	99.97	99.86	99.89	100.00	100.00
Fallow	100.00	100.00	99.61	100.00	100.00
Fallow_rough_plow	99.89	99.50	99.50	99.53	95.54
Fallow_smooth	99.58	99.44	98.35	99.67	99.39
Stubble	100.00	100.00	99.97	100.00	99.93
Celery	99.95	99.94	100.00	100.00	99.94
<b>Grapes_untrained</b>	97.82	87.20	88.68	92.34	95.61
Soil_vinyard Develop	99.99	100.00	98.33	99.99	99.97
Corn_senesced_green_weeds	99.90	99.09	98.60	99.44	98.98
Lettuce_romaine_4wk	100.00	100.00	99.53	100.00	99.88
Lettuce_romaine_5wk	99.98	100.00	100.00	100.00	100.00
Lettuce_romaine_6wk	100.00	100.00	99.44	99.50	99.09
Lettuce_romaine_7wk	99.90	99.54	98.97	99.63	98.00
<b>Vinyard_untrained</b>	99.22	96.87	83.53	90.79	98.14
Vinyard_vertical_trellis	99.99	99.88	99.32	99.99	99.95
OA(%)	99.38	96.66	94.80	96.98	98.53
AA(%)	99.76	98.83	97.73	98.81	99.02
$\kappa$	0.9930	0.9627	0.9418	0.9662	0.9835

Table 6: Classification accuracies (averaged over 5 runs) of MASR, PPF, ANNC-ASSCC and CSFF on Pavia Centre

	MASR	PPF	ANNC-ASSCC	CSFF
Water	99.87	99.15	100.00	100.00
Trees	94.22	97.96	98.75	98.75
Asphalt	99.45	97.37	99.26	98.61
Self-Blocking Bricks	99.98	99.27	99.96	99.93
Bitumen	98.75	98.79	99.35	99.69
Tiles	80.23	98.95	99.73	99.56
Shadows	99.34	94.36	97.49	98.21
Meadows	99.90	99.90	99.99	99.90
Bare Soil	84.80	99.96	98.72	99.99
OA(%)	98.02	99.03	99.73	99.75
AA(%)	95.17	98.41	99.25	99.40
$\kappa$	0.9719	0.9862	0.9961	0.9964

- [3] A. Villa, J. A. Benediktsson, J. Chanussot, and C. Jutten, “Hyperspectral image classification with independent component discriminant analysis,” *IEEE Transactions on Geoscience and Remote Sensing*, vol. 49, no. 12, pp. 4865–4876, Dec. 2011.
- [4] T. V. Bandos, L. Bruzzone, and G. Camps-Valls, “Classification of hyperspectral images with regularized linear discriminant analysis,” *IEEE Transactions on Geoscience and Remote Sensing*, vol. 47, no. 3, pp. 862–873, Mar. 2009.
- [5] F. Melgani and L. Bruzzone, “Classification of hyperspectral remote sensing images with support vector machines,” *IEEE Transactions on Geoscience and Remote Sensing*, vol. 42, no. 8, pp. 1778–1790, Aug. 2004.
- [6] D. Lunga, S. Prasad, M. M. Crawford, and O. Ersoy, “Manifold-learning-based feature extraction for classification of hyperspectral data: A review of advances in manifold learning,” *IEEE Signal Processing Magazine*, vol. 31, no. 1, pp. 55–66, Jan. 2014.

Table 7: Classification accuracies (averaged over 5 runs) of  $k$ NN, SVM and center classifier on spectral-spatial feature of Pavia University scene

	$k$ NN ( $k = 5$ )	$k$ NN ( $k = 10$ )	SVM	C-Classifier
Asphalt	98.69	98.69	98.40	98.46
Meadows	99.79	99.82	99.79	99.79
Gravel	96.40	96.15	95.90	96.03
Trees	97.99	97.90	97.93	98.00
Painted metal sheets	99.96	99.96	99.96	99.96
Bare Soil	100.00	100.00	100.00	100.00
Bitumen	98.86	98.84	98.88	98.91
Self-Blocking Bricks	94.57	94.78	95.33	95.21
Shadows	100.00	100.00	100.00	100.00
OA(%)	98.90	98.91	98.89	98.90
AA(%)	98.47	98.46	98.47	98.49
$\kappa$	0.9852	0.9853	0.9851	0.9852

Table 8: Classification accuracies (averaged over 5 runs) of  $k$ NN, SVM and center classifier on spectral-spatial feature of Salinas scene

	$k$ NN ( $k = 5$ )	$k$ NN ( $k = 10$ )	SVM	C-Classifier
Brocoli_green_weeds_1	100.00	100.00	99.97	99.97
Brocoli_green_weeds_2	100.00	100.00	100.00	100.00
Fallow	100.00	100.00	100.00	100.00
Fallow_rough_plow	93.36	95.51	95.56	95.54
Fallow_smooth	99.08	99.17	99.42	99.39
Stubble	99.91	99.92	99.92	99.93
Celery	99.93	99.94	99.94	99.94
Grapes_untrained	88.04	90.60	97.18	95.61
Soil_vinyard Develop	99.95	99.97	99.97	99.97
Corn_senesced_green_weeds	99.21	99.04	98.92	98.98
Lettuce_romaine_4wk	99.93	99.93	99.86	99.88
Lettuce_romaine_5wk	100.00	100.00	100.00	100.00
Lettuce_romaine_6wk	98.56	98.64	99.12	99.09
Lettuce_romaine_7wk	98.26	98.02	98.05	98.00
Vinyard_untrained	97.61	97.34	95.59	98.14
Vinyard_vertical_trellis	99.95	99.95	99.95	99.95
OA(%)	96.75	97.31	98.51	98.53
AA(%)	98.36	98.63	98.97	99.02
$\kappa$	0.9636	0.9699	0.9833	0.9835

Table 9: Classification accuracies (averaged over 5 runs) of  $k$ NN, SVM and center classifier on spectral-spatial feature of Pavia Centre scene

	$k$ NN ( $k = 5$ )	$k$ NN ( $k = 10$ )	SVM	C-Classifier
Water	99.99	99.99	99.99	100.00
Trees	98.92	98.93	98.74	98.75
Asphalt	98.45	98.27	98.71	98.61
Self-Blocking Bricks	99.89	99.92	99.93	99.93
	99.78	99.77	99.62	99.69
	99.31	99.44	99.56	99.56
	98.85	98.50	98.19	98.21
	99.88	99.88	99.89	99.90
	99.99	99.99	99.99	99.99
	OA(%)	99.77	99.75	99.75
	AA(%)	99.45	99.41	99.40
	$\kappa$	0.9967	0.9965	0.9964

- [7] B. C. Kuo, C. H. Li, and J. M. Yang, “Kernel nonparametric weighted feature extraction for hyperspectral image classification,” *IEEE Transactions on Geoscience and Remote Sensing*, vol. 47, no. 4, pp. 1139–1155, Apr. 2009.
- [8] B. Schölkopf and A. J. Smola, *Learning with kernels: support vector machines, regularization, optimization, and beyond*. Cambridge, MA: MIT press, 2002.
- [9] M. Fauvel, Y. Tarabalka, J. A. Benediktsson, J. Chanussot, and J. C. Tilton, “Advances in spectral-spatial classification of hyperspectral images,” *Proceedings of the IEEE*, vol. 101, no. 3, pp. 652–675, Mar. 2013.
- [10] Y. Chen, N. M. Nasrabadi, and T. D. Tran, “Hyperspectral image classification using dictionary-based sparse representation,” *IEEE Transactions on Geoscience and Remote Sensing*, vol. 49, no. 10, pp. 3973–3985, Oct. 2011.
- [11] M. Fauvel, J. A. Benediktsson, J. Chanussot, and J. R. Sveinsson, “Spectral and spatial classification of hyperspectral data using svms and morphological profiles,” *IEEE Transactions on Geoscience and Remote Sensing*, vol. 46, no. 11, pp. 3804–3814, Nov. 2008.
- [12] L. Z. Huo and P. Tang, “Spectral and spatial classification of hyperspectral data using svms and gabor textures,” in *Proceedings of the IEEE International Geoscience and Remote Sensing Symposium*, Jul. 2011, pp. 1708–1711.
- [13] J. Li, J. M. Bioucas-Dias, and A. Plaza, “Spectral-spatial classification of hyperspectral data using loopy belief propagation and active learning,” *IEEE Transactions on Geoscience and Remote Sensing*, vol. 51, no. 2, pp. 844–856, Feb. 2013.
- [14] A. Plaza, J. Plaza, and G. Martin, “Incorporation of spatial constraints into spectral mixture analysis of remotely sensed hyperspectral data,” in *Proceedings of the IEEE International Workshop on Machine Learning for Signal Processing*, Sep. 2009, pp. 1–6.
- [15] B. Song, J. Li, M. D. Mura, P. Li, A. Plaza, J. M. Bioucas-Dias, J. A. Benediktsson, and J. Chanussot, “Remotely sensed image classification using sparse representations of morphological attribute profiles,” *IEEE Transactions on Geoscience and Remote Sensing*, vol. 52, no. 8, pp. 5122–5136, Aug. 2014.
- [16] L. Fang, S. Li, X. Kang, and J. A. Benediktsson, “Spectral-spatial hyperspectral image classification via multiscale adaptive sparse representation,” *IEEE Transactions on Geoscience and Remote Sensing*, vol. 52, no. 12, pp. 7738–7749, Dec. 2014.
- [17] T. Hill, L. Marquez, M. O’Connor, and W. Remus, “Artificial neural network models for forecasting and decision making,” *International Journal of Forecasting*, vol. 10, no. 1, pp. 5–15, 1994.

- [18] G. P. Zhang, “Neural networks for classification: a survey,” *IEEE Transactions on Systems, Man, and Cybernetics, Part C (Applications and Reviews)*, vol. 30, no. 4, pp. 451–462, Nov. 2000.
- [19] A. Krizhevsky, I. Sutskever, and G. E. Hinton, “Imagenet classification with deep convolutional neural networks,” in *Advances in neural information processing systems*, 2012, pp. 1097–1105.
- [20] J. Schmidhuber, “Deep learning in neural networks: An overview,” *Neural Networks*, vol. 61, no. Supplement C, pp. 85–117, 2015.
- [21] J. A. Benediktsson, J. A. Palmason, and J. R. Sveinsson, “Classification of hyperspectral data from urban areas based on extended morphological profiles,” *IEEE Transactions on Geoscience and Remote Sensing*, vol. 43, no. 3, pp. 480–491, Mar. 2005.
- [22] Y. Chen, Z. Lin, X. Zhao, G. Wang, and Y. Gu, “Deep learning-based classification of hyperspectral data,” *IEEE Journal of Selected Topics in Applied Earth Observations and Remote Sensing*, vol. 7, no. 6, pp. 2094–2107, Jun. 2014.
- [23] Y. Chen, X. Zhao, and X. Jia, “Spectral-spatial classification of hyperspectral data based on deep belief network,” *IEEE Journal of Selected Topics in Applied Earth Observations and Remote Sensing*, vol. 8, no. 6, pp. 2381–2392, Jun. 2015.
- [24] V. Slakovikj, S. Verstockt, W. De Neve, S. Van Hoecke, and R. Van de Walle, “Hyperspectral image classification with convolutional neural networks,” in *Proceedings of the ACM international conference on Multimedia*. ACM, 2015, pp. 1159–1162.
- [25] Y. Chen, H. Jiang, C. Li, X. Jia, and P. Ghamisi, “Deep feature extraction and classification of hyperspectral images based on convolutional neural networks,” *IEEE Transactions on Geoscience and Remote Sensing*, vol. 54, no. 10, pp. 6232–6251, Oct. 2016.
- [26] H. Liang and Q. Li, “Hyperspectral imagery classification using sparse representations of convolutional neural network features,” *Remote Sensing*, vol. 8, no. 2, p. 99, 2016.
- [27] W. Zhao and S. Du, “Spectral-spatial feature extraction for hyperspectral image classification: A dimension reduction and deep learning approach,” *IEEE Transactions on Geoscience and Remote Sensing*, vol. 54, no. 8, pp. 4544–4554, Aug. 2016.
- [28] A. Romero, C. Gatta, and G. Camps-Valls, “Unsupervised deep feature extraction for remote sensing image classification,” *IEEE Transactions on Geoscience and Remote Sensing*, vol. 54, no. 3, pp. 1349–1362, Mar. 2016.
- [29] S. Yu, S. Jia, and C. Xu, “Convolutional neural networks for hyperspectral image classification,” *Neurocomputing*, vol. 219, pp. 88–98, 2017.
- [30] L. Jiao, M. Liang, H. Chen, S. Yang, H. Liu, and X. Cao, “Deep fully convolutional network-based spatial distribution prediction for hyperspectral image classification,” *IEEE Transactions on Geoscience and Remote Sensing*, vol. 55, no. 10, pp. 5585–5599, Oct. 2017.
- [31] K. Nogueira, O. A. B. Penatti, and J. A. D. Santos, “Towards better exploiting convolutional neural networks for remote sensing scene classification,” *Pattern Recognition*, vol. 61, pp. 539–556, 2017.
- [32] A. J. Guo and F. Zhu, “Spectral-spatial feature extraction and classification by ann supervised with center loss in hyperspectral imagery,” *arXiv preprint arXiv:1711.07141*, 2017.
- [33] W. Li, G. Wu, F. Zhang, and Q. Du, “Hyperspectral image classification using deep pixel-pair features,” *IEEE Transactions on Geoscience and Remote Sensing*, vol. 55, no. 2, pp. 844–853, Feb. 2017.
- [34] Y. Jia, E. Shelhamer, J. Donahue, S. Karayev, J. Long, R. Girshick, S. Guadarrama, and T. Darrell, “Caffe: Convolutional architecture for fast feature embedding,” in *Proceedings of the ACM International Conference on Multimedia*. ACM, 2014, pp. 675–678.

- [35] M. Abadi, A. Agarwal, P. Barham, E. Brevdo, Z. Chen, C. Citro, G. S. Corrado, A. Davis, J. Dean, M. Devin *et al.*, “Tensorflow: Large-scale machine learning on heterogeneous distributed systems,” *arXiv preprint arXiv:1603.04467*, 2016.
- [36] N. S. Altman, “An introduction to kernel and nearest-neighbor nonparametric regression,” *The American Statistician*, vol. 46, no. 3, pp. 175–185, 1992.
- [37] C.-C. Chang and C.-J. Lin, “Libsvm: A library for support vector machines,” *ACM Trans. Intell. Syst. Technol.*, vol. 2, no. 3, pp. 27:1–27:27, May 2011.
- [38] S. J. Pan and Q. Yang, “A survey on transfer learning,” *IEEE Transactions on Knowledge and Data Engineering*, vol. 22, no. 10, pp. 1345–1359, Oct 2010.